



Glucose Infusion Induced Change in Intracellular pH and Its Relationship with Tumor Glycolysis in a C6 Rat Model of Glioblastoma

Qi Qi^{1,2,3} · Matthew S. Fox^{3,4} · Heeseung Lim^{1,5} · Rebecca Sullivan^{2,4,6} · Alex Li⁵ · Miranda Bellyou⁵ · Lise Desjardins⁴ · Andrew McClennan^{1,4} · Robert Bartha^{1,2,5,7} · Lisa Hoffman^{1,2,4,6,8} · Timothy J. Scholl^{1,2,4,9} · Ting-Yim Lee^{1,2,4,5,7} · Jonathan D. Thiessen^{1,2,4,7}

Received: 5 November 2021 / Revised: 12 March 2022 / Accepted: 25 March 2022 / Published online: 23 November 2022
© The Author(s), under exclusive licence to World Molecular Imaging Society 2022

Abstract

Introduction The reliance on glycolytic metabolism is a hallmark of tumor metabolism. Excess acid and protons are produced, leading to an acidic tumor environment. Therefore, we explored the relationship between the tumor glycolytic metabolism and tissue pH by comparing ¹⁸F-fluorodeoxyglucose positron emission tomography (FDG-PET) and hyperpolarized [1-¹³C]pyruvate MR spectroscopy imaging (MRSI) to chemical exchange saturation transfer (CEST) MRI measurements of tumor pH.

Methods 10⁶ C6 glioma cells were implanted in the brains of male Wistar rats (*N* = 11) using stereotactic surgery. A 60-min PET acquisition after a bolus of FDG was performed at 11–13 days post implantation, and standardized uptake value (SUV) was calculated. CEST measurements were acquired the following day before and during constant infusion of glucose solution. Tumor intracellular pH (pH_i) was evaluated using amine and amide concentration-independent detection (AACID) CEST MRI. The change of pH_i (Δ pH_i) was calculated as the difference between pH_i pre- and during glucose infusion. Rats were imaged immediately with hyperpolarized [1-¹³C]pyruvate MRSI. Regional maps of the ratio of Lac:Pyr were acquired. The correlations between SUV, Lac:Pyr ratio, and Δ pH_i were evaluated using Pearson's correlation.

Results A decrease of 0.14 in pH_i was found after glucose infusion in tumor region. Significant correlations between tumor glycolysis measurements of Lac:Pyr and Δ pH_i within the tumor ($\rho = 0.83$, *P* = 0.01) and peritumoral region ($\rho = 0.76$, *P* = 0.028) were observed. No significant correlations were found between tumor SUV and Δ pH_i within the tumor ($\rho = -0.45$, *P* = 0.17) and peritumor regions ($\rho = -0.6$, *P* = 0.051).

Conclusion AACID detected the changes in pH_i induced by glucose infusion. Significant correlations between tumor glycolytic measurement of Lac:Pyr and tumoral and peritumoral pH_i and Δ pH_i suggest the intrinsic relationship between tumor glycolytic metabolism and the tumor pH environment as well as the peritumor pH environment.

Key words Tumor glycolytic metabolism · Tissue pH · Glucose solution

✉ Jonathan D. Thiessen
jthiessen@lawsonimaging.ca

¹ Department of Medical Biophysics, The University of Western Ontario, London, ON N6A 3K7, Canada

² Molecular Imaging Program, The University of Western Ontario, London, ON N6A 3K7, Canada

³ Department of Physics and Astronomy, The University of Western Ontario, London, ON N6A 3K7, Canada

⁴ Imaging Program, Lawson Health Research Institute, London, ON N6A 4V2, Canada

⁵ Robarts Research Institute, The University of Western Ontario, London, ON N6A 3K7, Canada

⁶ Department of Pathology, The University of Western Ontario, London, ON N6A 3K7, Canada

⁷ Department of Medical Imaging, The University of Western Ontario, London, ON N6A 3K7, Canada

⁸ Department of Anatomy and Cell Biology, The University of Western Ontario, London, ON N6A 3K7, Canada

⁹ Ontario Institute for Cancer Research, Toronto, ON M5G 0A3, Canada

Introduction

Tumor pH and metabolism are intrinsically related. Changes in the tumor pH environment as a result of metabolism could provide crucial information on its aggressiveness and progression [1–4]. In general, the tumor extracellular pH (pH_e) environment is more acidic than intracellular pH (pH_i) as a result of the overreliance on aerobic glycolysis, through which excess lactic acid and H^+ are produced and transported to the extracellular space to maintain a more alkaline pH_i , which avoids apoptosis [1, 2, 5, 6]. pH_e can be measured *in vivo* using techniques such as pH probes, chemical exchange saturation transfer (CEST) in conjunction with exogenous contrast agents, and magnetic resonance spectroscopy imaging (MRSI) using hyperpolarized bicarbonate [3, 5–7]. However, the *in vivo* information on pH_i is often missing as it is challenging to obtain information from the intracellular space. Importantly, an alteration in tumor pH_i could provide crucial information about treatment response [6, 10]. Previously, an infusion of glucose was found to decrease pH_e in human tumor xenografts [8]. In fact, most tumors rely on aerobic glycolysis for energy production (also known as “the Warburg effect”), resulting in increased production of H^+ and lactate acid that are extruded to the extracellular space [4]. Tumoral and peritumoral regions are intrinsically related, with tumor metabolism also able to alter the peritumoral pH microenvironment. pH in the peritumoral region could potentially indicate the level of tumor activity or aggression [3]. Lower pH_i in the peritumoral region could be due to a high concentration of hydrogen ions produced by highly active tumor cells. Information on tumor metabolism can be acquired by evaluating the change in tumor pH environment induced by an injection or infusion of glucose.

A CEST MRI method based on the distinct CEST responses of the endogenous amide and amine proton that are available in tumor intracellular space enables the measurement of *in vivo* pH_i [11]. Amide and amine concentration-independent detection (AACID) was developed exploiting the change in exchange rate of amide and amine proton due to change in pH_i [11]. The ratio of amide-to-amine CEST effect can be calculated and then related to pH_i [10, 11], where higher AACID values are associated with lower pH_i . However, whether AACID can still evaluate pH_i and the change in pH_i in a system with metabolites that possess similar resonant frequencies to amine or amide remained to be tested. Tumor glycolytic metabolism can be evaluated with positron emission tomography (PET) and ^{18}F -fluorodeoxyglucose (FDG), a glucose analogue that is phosphorylated to FDG-6-phosphate (FDG6P) after the first step of glycolysis but doesn't go

through subsequent steps. As a result, FDG6P becomes trapped inside cells. Anaerobic glycolysis can also be measured with magnetic resonance spectroscopy imaging (MRSI) by monitoring the conversion to pyruvate during anaerobic glycolysis to lactate after an injection of hyperpolarized $[1-^{13}\text{C}]$ pyruvate [12].

The purpose of this study was to test whether AACID CEST can still detect the change in pH_i in the presence of glucose and explore the relationship between tumoral, peritumoral pH_i , and the change in pH_i after a glucose infusion using AACID CEST MRI and tumoral glycolytic activity measured using FDG-PET and hyperpolarized $[1-^{13}\text{C}]$ pyruvate MRSI. Intracellular pH measurements were made following perfusion of glucose and related to previously published measures of glycolysis [13]. We hypothesized that tumoral and peritumoral pH_i are inversely proportional to tumor glycolysis measurements and the change in tumoral and peritumoral pH_i induced by glucose infusion is directly proportional to tumor glycolysis measurements.

Methods

Experiment Design

Detailed experimental protocols and procedures can be found in a previous publication [13]. All procedures were performed in compliance with the Canadian Council for Animal Care (CCAC) and approved by the Western University Animal Care Committee (ACC). A sample size of 10 was required to detect a pH change in tumor environment from >7.1 to 6.8 [6] with a standard deviation of 0.3 to achieve a power of 80% using an online software (experimental design assistant, <https://eda.nc3rs.org.uk/eda/login/auth>). A sample size of 11 was decided considering potential failure during the experiment process, no control group and exclusion criteria were used as this preliminary study was designed to explore the capability of the AACID pH imaging technique in the presence of glucose. All 11 male Wistar rats were treated and cared equally in compliance with CCAC and ACC guidelines and completed all experimental procedures. In short, C6 glioma tumor cells were implanted on day 0 on all 11 male Wistar rats followed by a CT perfusion check on day 7 to confirm tumor growth (tumor longest axis ≥ 4 mm) [13, 14]. After confirming the longest axis of tumor had reached 4 mm, the FDG-PET experiment was performed between day 11 and 13 after C6 cell implantation. MRI experiments (CEST followed by hyperpolarized $[1-^{13}\text{C}]$ pyruvate MRSI) were performed on the next day immediately prior to euthanasia with all imaging experiments taking place within a span of 24 h for each animal. Rats were anesthetized with isoflurane for all experimental procedures.

C6 glioma Model

A detailed description of the C6 glioma model can be found in previous publications [13, 14].

Wild-type male Wistar rats (Charles River, Canada, age 8 to 10 weeks at surgery) weighing on average 401 ± 42 g ($N=11$) were used in this study. No previous procedures were performed on these rats prior to the study. The stereotactic surgical process for glioma cell implantation took place at the animal care facility in the Lawson Health Research Institute. The animals were induced with 5% isoflurane and were maintained at 2% during the surgery. A burr hole was drilled at a point 1 mm anterior and 3 mm to the right of the bregma after an incision on the skull to expose the bregma. One million C6 glioma cells (CCL-107, American Type Culture Collection, Manassas, VA) were cultured [13, 15] and injected at the location of the burr hole at a depth of 3–4 mm from the skull surface with a Hamilton syringe. The burr hole was filled with bone wax, and the incision was sutured. Animals were recovered and returned to animal facility for housing after the surgeries. Metacam (Boehringer Ingelheim Vetmedica Inc., Duluth, USA, 10 mg/kg) was administered prior to surgery and 12 h after surgical recovery to relieve pain and reduce inflammation.

FDG-PET Imaging

The detailed PET procedure can be found in a previous publication [13]. In short, the PET acquisitions of tumor glycolysis of the 11 male Wistar rats were performed using a small animal PET system (Inveon DPET, Siemens Healthineers, Knoxville, TN, USA) between day 11 and 13 after C6 cell implantation. The animals were induced with 5% isoflurane and were maintained at 2% during image acquisition. The blood glucose of each subject was measured and reported in previous work [13] by taking blood from a lateral tail vein prior to an injection. Each subject was injected with a bolus of ^{18}F -FDG (31.5 ± 3.1 MBq) intravenously 30 s after the start of the 75 min dynamic PET acquisition. The PET data was reconstructed using a CT-based attenuation correction map and an iterative, 3D ordered subset expectation maximization with 2 iterations and 18 subsets.

Standardized uptake values (SUV) were calculated using the last 15 min of the PET images as a measurement of glycolysis [13, 16].

Dynamic CEST Imaging

A detailed description of the CEST procedure can also be found in a previous publication [13]. The CEST MRI of tumor pH environment was acquired on a 9.4-T small animal MRI (Agilent, Palo Alto, CA, USA) on the morning after the PET acquisition (12–14 days after the surgery).

MRI images of all 11 male Wistar rats were acquired on a 9.4-T small animal MRI scanner (Agilent, Palo Alto, CA, USA) equipped with a 15-cm gradient coil set of 450 mT/m strength, Bruker Avance MRI III console with software package of Paravision-6 (Bruker BioSpin Corp, Billerica, MA). Rats were induced with 5% isoflurane and were maintained at 2% during MRI acquisition. Standard anatomical T_2 -weighted images were used for tumor detection. The T_2 -weighted images were acquired using a 2-dimensional TurboRARE pulse sequence with parameters: TR/TE = 5000/40 ms, FOV = 38.4×38.4 mm², matrix size = 192×192 , 31 slices with slice thickness = 1 mm. Upon initial tumor detection, a 2-mm slice from the T_2 -weighted images with maximum tumor coverage was selected for CEST imaging. CEST imaging was acquired using a 2-dimensional RARE pulse sequence (TR/TE = 10,000/25 ms, FOV = 38.4×38.4 mm², matrix size = 96×96 , slice thickness = 2 mm) preceded by a continuous RF pulse with amplitude 1.5- μT and duration 4 s. The CEST images were acquired at different saturation frequencies (–5.0 to 5.0 ppm with 0.2 ppm increment); –1000 and 1000 ppm images were acquired as reference, total 53 images. Three consecutive spectra were obtained with 30 min per CEST acquisition. A baseline CEST spectrum was acquired prior to an infusion. A bolus of 20% of D-glucose by weight dissolved in saline solution (0.3 g/kg) was injected after the baseline CEST spectrum, followed by a 60-min constant infusion of the same 20% D-glucose solution (1.5 g/kg/h). The acquisition of the second and third CEST spectra was associated with the first and second half of glucose constant infusion with 30-min duration each, respectively. The third CEST spectrum was denoted as “during infusion” and used to compare with the baseline CEST spectrum to examine the effect of glucose infusion on pH_i using AACID. The CEST signal from glucose may not be relevant to the AACID evaluation as only amine and amide resonant frequencies were used for analysis.

Hyperpolarized [$1\text{-}^{13}\text{C}$]Pyruvate

Detailed procedures for hyperpolarized [$1\text{-}^{13}\text{C}$]pyruvate MRSI of tumor aerobic glycolysis can be found in previous publications [12, 13].

Briefly, the male Wistar rats ($N=11$) were transferred under 2% isoflurane to a 3.0 T MRI system (GE Discovery MR750, General Electric Healthcare, Waukesha WI, USA) for the hyperpolarized [$1\text{-}^{13}\text{C}$]pyruvate MRSI experiment immediately after the CEST experiment. An FSE sequence was used to locate and acquire a T_2 -weighted MRI of the same slice used for the CEST acquisition (80×80 mm FOV, 0.3-mm in-plane resolution, 3-mm slice thickness, TR = 4000 ms, TE = 85 ms, 16 echo trains, number of averages = 9). A volume of 3 mL hyperpolarized [$1\text{-}^{13}\text{C}$]pyruvate

solution was injected through a rat lateral tail vein by a single bolus in 12 s. Axial ^{13}C spectra were acquired using a 2D free induction decay chemical shift imaging (FID-CSI) pulse sequence (FOV = 60×60 mm, slice thickness approximately equal to the tumor extent, 12×12 spectral imaging matrix, TR = 80 ms, bandwidth = 5 kHz, 2048 pts, flip angle = 10°) 13 s after injection to complete the circulation and metabolism of hyperpolarized [$1\text{-}^{13}\text{C}$]pyruvate. Each FID-CSI containing 144 spectra was acquired within a total scan time of 12 s. Maps of the ratio of lactate to pyruvate (Lac:Pyru) were derived as a measurement of anaerobic glycolytic metabolism using a customized MATLAB script [12, 13]. The animal was euthanized immediately at the end of the experiment with an overdose of isoflurane.

Phantom Preparation

Phantoms were made following the recipe from McVicar et al. [11] to imitate physiological protein and glucose concentration in rodent and human brain. Bovine serum albumin powder (BSA, Sigma-Aldrich, St. Louis, Missouri, US) and glucose powder (D-(+)-glucose, Sigma-Aldrich, St. Louis, Missouri, US) were prepared in pH buffer solutions to achieve 10% BSA and the required glucose concentrations (2.5, 4.5 and 6 mM). Series of pH buffers were made by adding HCl and NaOH to $1 \times$ phosphate-buffered saline (PBS) solution to obtain physiological pH levels of 6.2, 6.4, 6.6, 6.8, 7.0, 7.2, and 7.4. The pH values were measured by using a benchtop pH meter (Accumet Basics AB15 pH meter, Fisher Scientific, Waltham, Massachusetts, USA). Three phantoms at glucose concentration of 2.5, 4.5, and 6 mM were made to mimic extracellular tissue glucose concentrations during normo- to hyperglycemic conditions in rat brain [17]. Each phantom contains 7 NMR tubes (3 mm diameter, Sigma-Aldrich, St. Louis, Missouri, USA) held by a custom 3D printed holder. The NMR tubes contain mixtures at pH of 6.2, 6.4, 6.6, 6.8, 7.0, 7.2, and 7.4. Phantoms were scanned using the same imaging protocol as the *in vivo* CEST experiment as described above.

Simulation

A 7-pool model was used to simulate AACID CEST signal (based on code available at cest.org), with the analytical solution derived from Bloch-McConnell equations as described by Zaiss et al. [18, 19]. Four pools were associated with glucose at resonant frequencies of 0.66, 1.29, 2.18, and 2.88 ppm (pool B, D, E, F respectively), 1 pool was associated with amine at 2.75 ppm (pool G), 1 pool was for amide at 3.5 ppm (pool H), and the water pool was set at 0 ppm (pool A). The macromolecule effect and nuclear overhauser effect (NOE) were neglected from the simulation. The exchange rates at different pH's for glucose at 4 resonant

frequencies could be defined using Eq. 1 according to Zaiss et al [18, 19]:

$$k_{XA} = k_{x1} \cdot 10^{\text{pH}-7} + k_{x0} \quad (1)$$

where k_{BA} , k_{DA} , k_{EA} , and k_{FA} ($x = B, D, E,$ and F) are the proton exchange rates for the 4 corresponding exchanging protons on D-glucose, and the exchange rates for amine and amide at Different pHs were defined as Eq. 2 and 3 based on McVicar et al. [11]:

$$k_{\text{amine}} = 10^{\text{pH}-4.2} \quad (2)$$

$$k_{\text{amide}} = 5.75 \times 10^{\text{pH}-6.4} \quad (3)$$

Relevant simulation parameters are listed in Table 1.

CEST Imaging Analysis

Custom scripts were written using MATLAB 2018b (MathWorks, Natick, Massachusetts USA) for all CEST analysis. A mask of the brain was delineated using the T_2 -weighted MR images and applied to the CEST images. The Z-spectra were fitted with method described in previous publication [13]; briefly, the data from each voxel was smoothed with a smoothing spline fit of a fitting parameter of 0.998. The frequency associated with the minima of Z-spectra were shifted to 0 ppm for B_0 correction. Magnetization transfer ratio asymmetry (MTR_{asym}) spectra were calculated as shown in Eq. 4.

$$\text{MTR}_{\text{asym}} = \frac{S(-\Delta\omega) - S(\Delta\omega)}{S_0} \quad (4)$$

Using the MTR_{asym} spectra, a Lorentzian line was fitted at the visible resonance frequencies of glucose, amine,

Table 1. Parameters used for the 7-pool simulation

Parameter	Value
T_1	2.002 s
T_2	0.2 s
B_0	9.4 T
B_1	1.5 μT
Glucose concentration	2.5, 4.5, and 6 mM
k_{B1}	1467 Hz
k_{B0}	617 Hz
k_{D1}	3580 Hz
k_{D0}	800 Hz
k_{E1}	2804 Hz
k_{E0}	669 Hz
k_{F1}	8543 Hz
k_{F0}	675 Hz

and amide. The amplitude and full-width half maximum (FWHM) were obtained from these Lorentzian curves; however, the effect of NOE was not identified in this estimation.

AACID maps were generated using a custom MATLAB script, with AACID values calculated based on Eq. 5 using method developed by McVicar et al. [11] (Figs. 1 and 2).

$$\text{AACID} = \frac{Mz_{(3.50\text{ppm})} \times (Mz_{(5\text{ppm})} - Mz_{(2.75\text{ppm})})}{Mz_{(2.75\text{ppm})} \times (Mz_{(5\text{ppm})} - Mz_{(3.50\text{ppm})})} \quad (5)$$

Estimation of pH_i Using AACID

The CEST data from the phantom was analyzed using the same method described above, the AACID values were

calculated, and the relationships between AACID and pH were evaluated and plotted at the three concentrations of 2.5, 4.5, and 6 mM that is comparable to brain glucose concentration during normoglycemia to hyperglycemia *in vivo* [17]. A linear relationship was fitted, and the goodness-of-fit (R^2) was reported between pH and AACID values at these glucose concentrations as shown in Fig. 3. An overall fit was also created by evaluating the relationship between pH and averaged AACID value from all 3 phantoms at its corresponding pH as shown in Fig. 3d. Differences between the linear correlation of pH and AACID were compared at the different glucose concentrations to determine whether glucose concentration affected the AACID measurements. The phantom calibration data were then used to estimate pH_i from the *in vivo* AACID values. The NOE effect was

Fig. 1. MTR_{asym} maps of phantom (6 mM) at the resonant frequencies of glucose of 0.66, 1.28, 2.18, and 2.88 ppm as well as the amine and amide resonant frequencies of 2.75 and 3.5 ppm.

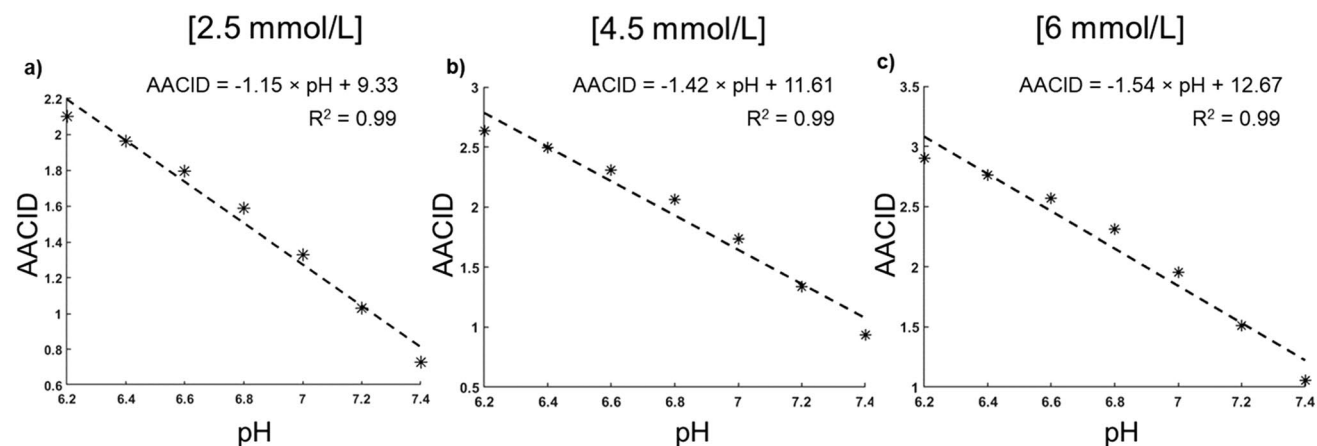
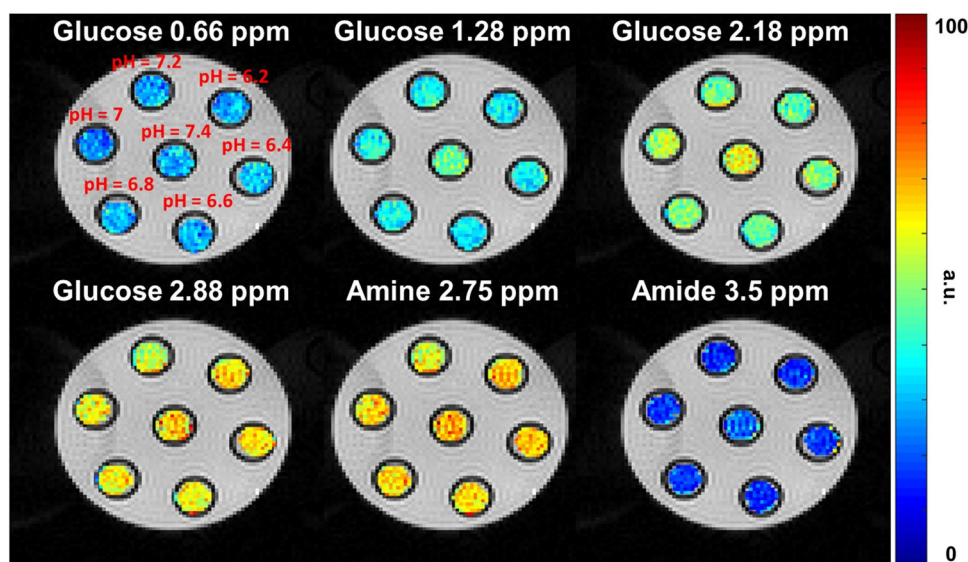


Fig. 2. The relationship between pH and AACID value from simulation using the 7-pool exchange model is plotted at glucose concentrations of 2.5 (a), 4.5 (b), and 6 mmol/L (c). The lines of best fit

are represented by the dotted line, and the fitting equations and the goodness-of-fit are shown at the top right corner of each plot.

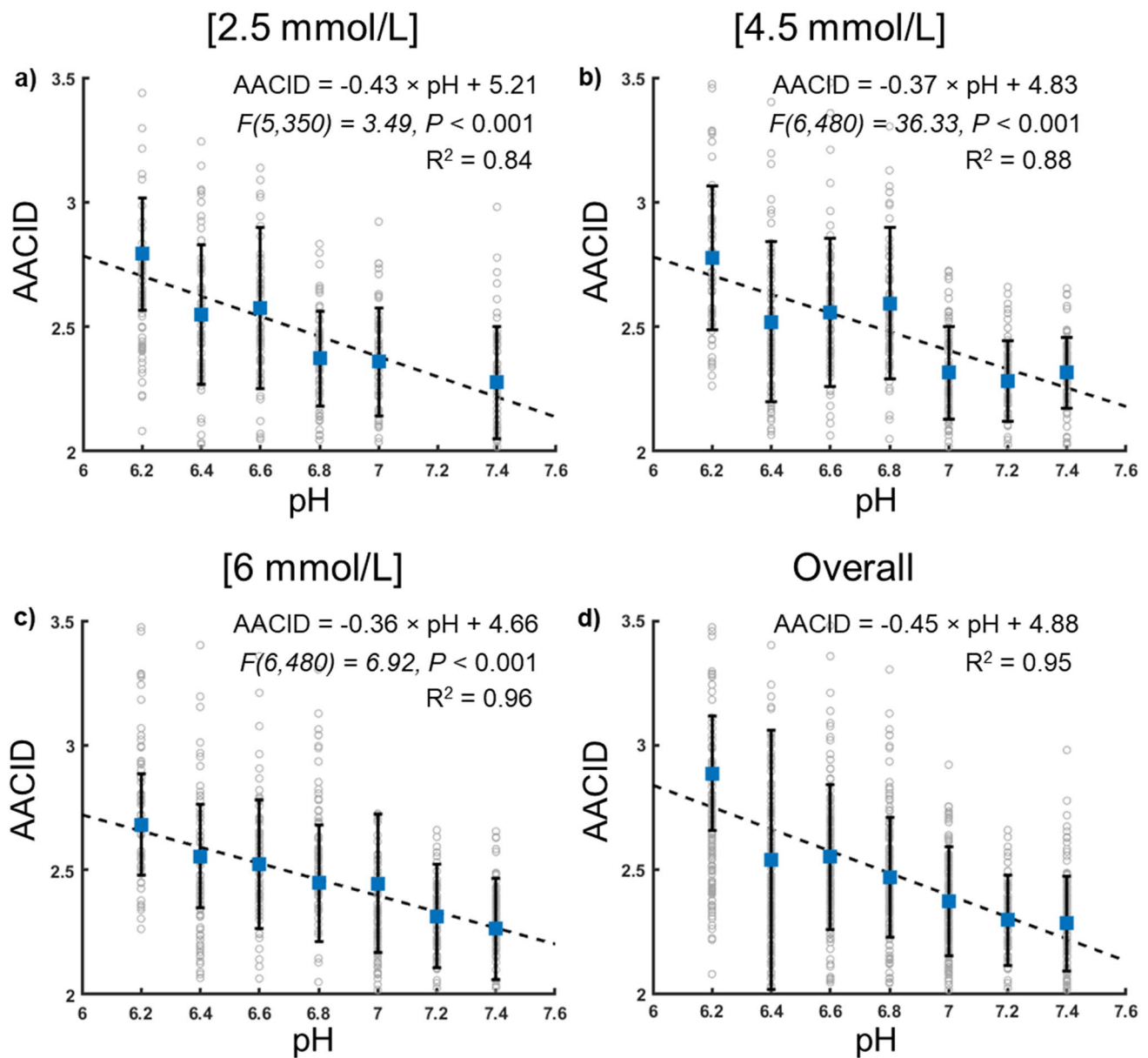


Fig. 3. pH vs. mean AACID value extracted from the ROI associated with each NMR tube on the AACID maps obtained from the phantom experiment at glucose concentrations of 2.5 (a), 4.5 (b), and 6 (c) mmol/L. pH vs. mean AACID values from all three concentrations are shown in (d). The blue square indicates the mean AACID value

at each pH value, the hollow gray circle indicates individual AACID value from each NMR ROI, the error bar denotes the standard deviation, and the dashed line indicates the line of best fit. The equation for the line of best fit, one-way ANOVA test results, and the goodness-of-fit are reported in the top right corner of each panel.

minimal to AACID calculation [11] in both phantom and in vivo experiments and neglected as AACID is independent of NOE as shown in Eq. 5.

Pixel-wise maps representing change in pH_i (ΔpH_i) were generated using Eq. 6 and the baseline intracellular pH gradient (pHG_i) was defined by Eq. 7:

$$\Delta pH_i = pH_i(\text{During}) - pH_i(\text{Pre}) \quad (6)$$

$$pHG_i = pH_i(\text{Tumor}) - pH_i(\text{Peritumor}) \quad (7)$$

ROI Selection and Image Registration

Detailed description of ROI analysis and image registration can be found in a previous publication [13]. T_2 -weighted MRI was used as guidance for manual delineation of tumor, peritumor (3 mm away from the tumor boundary within the same hemisphere [15, 20]) and contralateral brain regions.

All voxels that contained tumor on the T_2 -weighted MRI were included in the tumor ROIs. The T_2 -weighted MRI was also used as a reference for manual rigid co-registration of CEST, FDG-PET, and hyperpolarized $[1-^{13}\text{C}]$ pyruvate images using 3D Slicer (www.slicer.org). ROI delineations using the T_2 -weighted image from the 9.4 T MRI were applied to all of the co-registered parameter maps (CEST, MRSI, and FDG-PET). The mean tumoral, peritumoral, and contralateral brain pH_i and ΔpH_i from CEST; tumor SUV from FDG-PET; and tumor Lac:Pyr ratios from hyperpolarized $[1-^{13}\text{C}]$ pyruvate MRSI were extracted.

Statistical Analysis

A paired sampled t test was used to investigate the effect of glucose infusion on mean pH_i in the tumor, peritumor, and contralateral brain of the 11 rats. A two-way ANOVA test was performed to determine if a simple main effect exists for tissue types (tumor, peritumor, and contralateral brain) and glucose infusion (pre- and during infusion) on pH_i evaluated by AACID CEST using IBM SPSS version 22. One-way ANOVA tests were performed to investigate the simple main effect of pH on AACID and the simple main effect of glucose concentration on AACID values. The Pearson correlations were computed between averaged tumor Lac:Pyr, SUV, and pH_i for tumoral and peritumoral tissues. A P value ≤ 0.05 was considered statistically significant. All statistical analysis was performed using IBM SPSS version 22.

Results

AACID vs. pH from Simulation

From the three glucose concentrations ranging from normoglycemia to hyperglycemia, inversely proportional relationships between pH and AACID were found among all three as shown in Fig. 2, with a higher AACID value associated with a lower pH value. R^2 of the linear fitting from simulation at glucose concentration of 2.5 (a), 4.5 (b), and 6 mM (c) are 0.99.

CEST Signal at Relevant Metabolite Resonance Frequencies

An illustrative example of the phantom MTR_{asym} maps at resonance frequencies of glucose, amide, and amine is shown in Fig. 1.

AACID Value vs. pH from Phantom

From normoglycemia to hyperglycemia using the same concentration as the simulation, an inversely proportional

relationship between pH and average AACID values is shown in Fig. 3 demonstrating a higher AACID value is associated with a lower pH under all three glucose concentrations. An inversely proportional relationship between AACID values and pH was found among all three glucose concentrations as shown in Fig. 3; the slopes, the y-intercepts, and the R^2 at each concentration also are displayed. A one-way ANOVA test indicated a simple main effect of pH on AACID value ($P < 0.05$). Glucose concentration did not indicate a simple main effect on AACID values ($P > 0.05$) from the one-way ANOVA test. As a result, the slope and intercept from the overall fitting were used to obtain an overall estimation of pH_i independent of glucose concentration (Fig. 3d).

Comparison Among Phantom and In Vivo AACID Values

The in vivo AACID values displayed a similar range as AACID values acquired from phantom measurements as shown in Table 2. The *in Vivo* AACID values were calibrated using the AACID values acquired from the phantom scan and the resulting average pH_i using the phantom calibration.

pH_i Change During Glucose Infusion

Box and whisker plots showing median pH_i before and during glucose infusion in tumoral, peritumoral, and contralateral tissue regions are shown in Fig. 4. Co-registered pH_i maps, SUV, and Lac:Pyr images are shown in Fig. 5. The change in averaged pH_i in tumor and peritumor region for individual subject ($N = 11$) can be found in Supplementary Fig. 4. After comparing the pH_i pre- and during infusion using a two-tailed paired-sample t test, a significant difference was found in the tumoral region ($P < 0.01$), whereas no significant change was found in the peritumoral ($P = 0.93$) or the contralateral brain region ($P = 0.30$). No simple main effects were found in pH_i for either tissue type ($P = 0.068$) or infusion ($P = 0.902$). pH_i detected in the three tissue types and as a function of glucose infusion (pre- and during infusion) are not significantly different as shown in Fig. 4.

Table 2. Range of AACID values from *in Vivo* and phantom measurements

	AACID range
<i>In Vivo</i> pre-infusion	0–2.89
<i>In Vivo</i> post-infusion	0–3.52
Phantom [2.5 mmol/L]	0–3.40
Phantom [4.5 mmol/L]	0–3.05
Phantom [6 mmol/L]	0–2.91

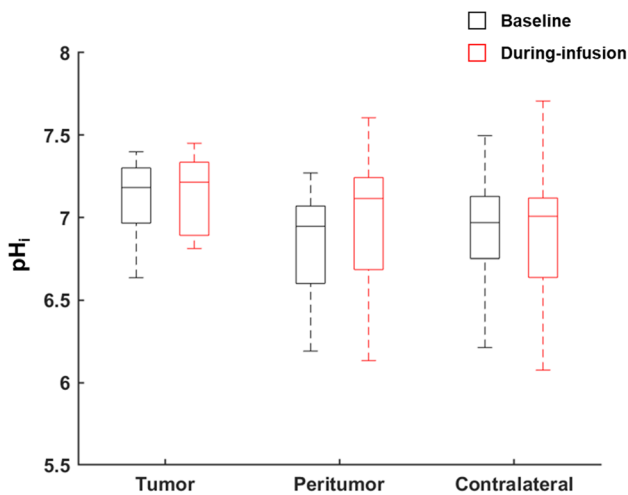


Fig. 4. Box and whisker plot illustrating the median pH_i at baseline and during infusion in the tumor, peritumor, and contralateral brain region. The line inside each box indicates the median of the AACID value from each NMR tube, the box indicates interquartile range (IQR), and the top and the bottom end of the error bar indicate the 75th percentile + 1.5 IQR and the 25th percentile, 1.5 IQR, respectively. No simple main effect was found for pH_i in these three regions at baseline or during infusion.

Tumor Glycolysis Measurements vs. *In Vivo* pH_i

Significant correlations between tumor Lac:Pyr and baseline tumoral pH_i ($\rho = -0.58$, $P = 0.04$) and peritumoral pH_i ($\rho = -0.66$, $P = 0.03$) are shown in Fig. 6a and b. Higher tumor Lac:Pyr is associated with lower tumoral and peritumoral pH_i . There is significant correlation between tumor Lac:Pyr and pHG_i from tumor–peritumor regions ($\rho = 0.57$, $P = 0.05$) (Supplementary Fig. 1). Higher tumor Lac:Pyr leads to higher pH_i gradient (tumor $\text{pH}_i >$ peritumor pH_i).

Significant correlations between tumoral Lac:Pyr and tumoral and peritumoral ΔpH_i ($\rho = 0.83$, $P = 0.01$; $\rho = 0.76$, $P = 0.03$ respectively) were also found as shown in Fig. 6c and d. Higher tumor Lac:Pyr leads to a greater increase in pH_i in tumoral and peritumoral regions during glucose infusion. However, no significant correlation was found between tumoral or peritumoral ΔpH_i with tumor SUV ($\rho = -0.45$, $P = 0.17$; $\rho = -0.6$, $P = 0.051$, respectively) as shown in Table 3.

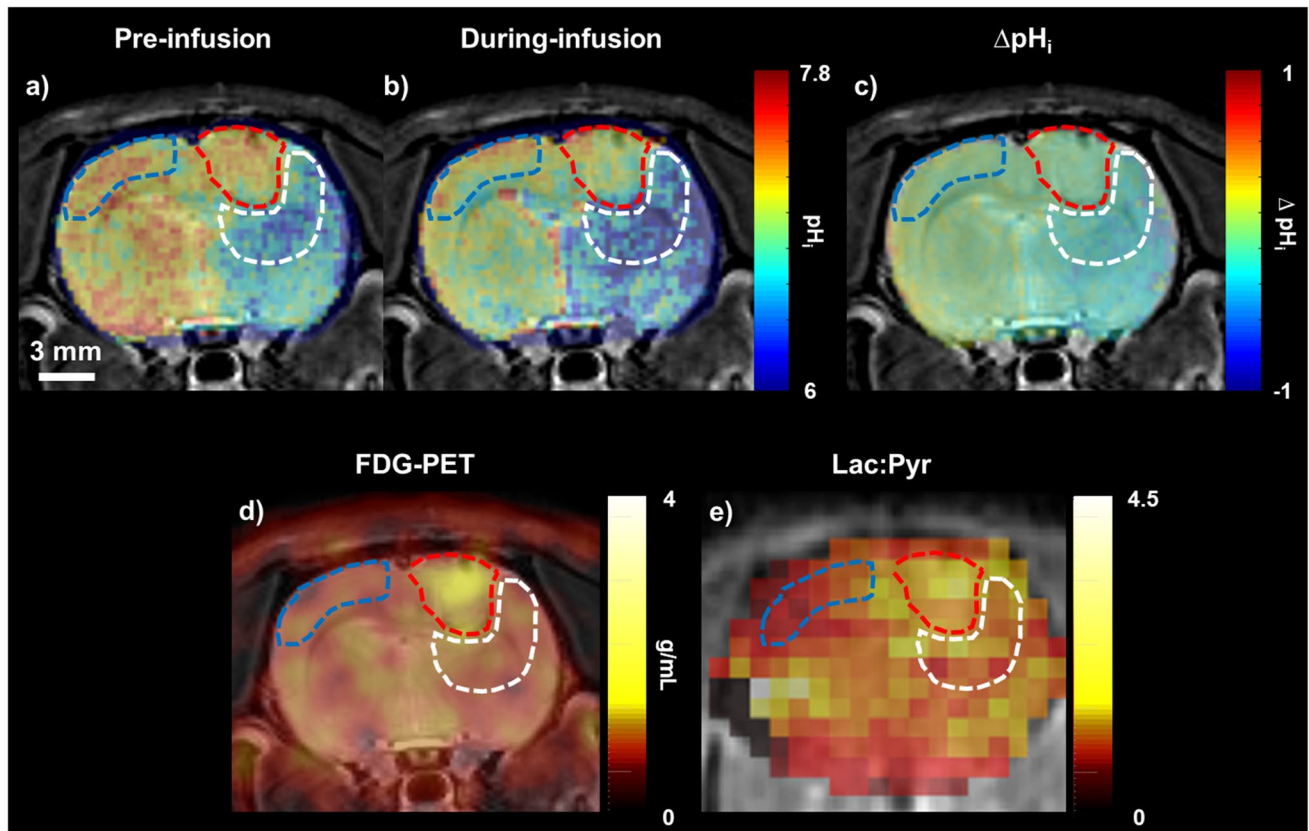


Fig. 5. An illustrative example of registered pH_i maps pre- (a), during infusion (b), ΔpH_i map (c), SUV map (d), and Lac:Pyr maps (e) overlaid on T_2 -weighted MRI. Tumor, peritumor, and contralateral brain regions are delineated by red-, white-, and blue-dotted lines, respectively.

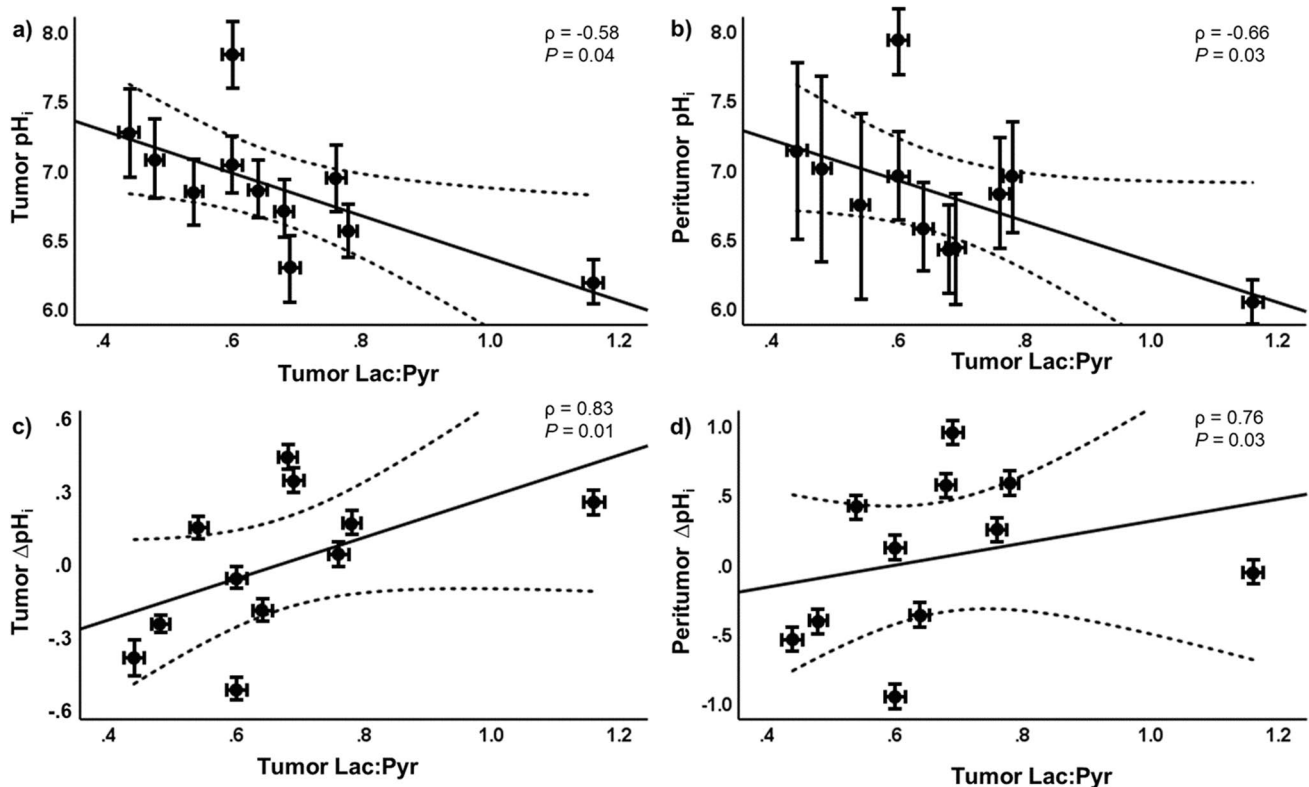


Fig. 6. The relationship between tumor Lac:Pyruvate and tumor baseline pH_i (a), peritumor baseline pH_i (b), tumoral ΔpH_i (c), and peritumoral ΔpH_i (d). Dotted lines indicate the 95% confidence interval, and the error bar denotes the standard deviation.

Table 3. Pearson's correlation among tumor glycolysis measurements (SUV and Lac:Pyruvate) and tumor and peritumor baseline pH_i , pHG_i , and ΔpH_i induced by glucose infusion. Asterisk indicates a statistical significance of $P < 0.05$

$N=11$	pH_i	pH_p	pHG_i	ΔpH_i	ΔpH_p
SUV	-0.33	-0.27	0.16	-0.45	-0.51
Lac:Pyruvate	-0.58*	-0.66*	0.57*	0.83*	0.76*

Discussion

Both phantom and simulation results indicated the inversely proportional relationship between pH and AACID values remains under normoglycemic to hyperglycemic conditions (as shown in Figs. 2 and 1), where higher AACID values are associated with lower pH values. These results agreed with previous publications [10, 11]. The results from both the phantom experiment and simulation confirmed that the relative change of AACID values before and after the glucose infusion captured the pH_i change *in Vivo*. The one-way ANOVA test from the phantom measurements indicated a simple main effect of pH on AACID values, but the glucose concentration did not have a simple main effect on the AACID values. This potentially

indicates that AACID values are independent of metabolite concentration, even in the presence of a metabolite (glucose) with a resonant frequency close to amine. Although no simple main effect was found when evaluating AACID values measured with different glucose concentrations, the slopes and y-intercepts are different when simulating three different concentrations of glucose. Because of the lack of significant effect of glucose concentration on AACID values, we combined the data from all phantom experiments to create an overall estimate of the slope and intercept to relate AACID to pH_i . It is worth noting that the slope and y-intercept from the current fitting are distinct from the reported slope (-0.64) and y-intercept (6.5) without the presence of glucose from the original AACID publication that used a FSE sequence of the same B_1 and RF duration [11]. Overall, although the glucose concentration does not have a simple main effect on AACID, a calibration experiment with phantom(s) mimicking the experimental microenvironment should be obtained prior to *in Vivo* experiments to ensure the accuracy of pH_i measurement using AACID CEST MRI.

The Lorentzian fitted lines on the MTR_{asym} spectra from the phantoms showed an increase in the FWHM for glucose peaks which was observed as pH increased (Supplementary Fig. 2). In a previous study, the direct proportional

relationship between FWHM of MTR_{asym} and the k_{ex} of the corresponding metabolite was demonstrated [21]. The increasing FWHM as pH increased from 6.2 to 7.4 confirmed the k_{ex} approximation using Eq. 1 for simulation.

As reported from a previous publication, the baseline blood glucose of this set of rats was 7.3 mmol/L and slowly increased to > 20 mmol/L when using the same infusion protocol on the benchtop [13]. This corresponds to brain glucose concentrations of approximately 1.8 mmol/L at baseline and > 5 mmol/L during infusion according to the estimation given by Silver et al. [17]; these glucose concentrations are comparable to the values used in the simulation and the phantom study. The pre-infusion tumor pH_i derived using the phantom calibration is 7.17 ± 0.29 , which is close to a previous study using the same tumor type and similar time post-surgery ($\text{pH}_i \approx 7.3$) [6]. AACID CEST was able to capture the changes in tumoral pH_i induced by glucose infusion, with pH_i in the tumor region significantly lower during infusion (7.03 ± 0.45) than pre-infusion. Decreased tumor pH_i after a glucose infusion can be attributed to the Warburg effect, with elevated glycolytic activity, especially under hyperglycemic conditions, resulting in the production of excess H^+ and lactate [2–4]. However, no significant changes of pH_i in peritumoral or contralateral brain regions were found from the paired sampled t test nor any significant difference was found among tumor, peritumor, and contralateral pH_i before and post-glucose infusion.

Studies have found that the tumor pH extracellular (pH_e) environment becomes more acidic towards the tumor edge and the peritumoral regions; this is the result of the elevated activation of glucose transporters and poor tumor perfusion [2, 3, 13–15]. This study demonstrated a similar pH_i distribution to previous measurements of pH_e [3], with lower peritumoral pH_i than tumor pH_i as shown in Fig. 5 (albeit, not statistically significant when measured in all 11 rats). This drop in peritumoral pH_i may indicate the area where intracellular acidosis has taken place [2], which is further highlighted after glucose infusion. The peritumor region would eventually be left vacant for glioma cells to invade, and this study may capture the process of glioma invasion to the peritumor region by displaying a lower pH_i in these regions relative to the surrounding tissue. The significant correlation between tumor Lac:Pyr and baseline tumor/peritumor pH_i emphasizes the effect of tumor anaerobic glycolysis on its pH environment. Higher tumor glycolytic activity has been associated with lower extracellular pH (pH_e) [1, 2, 6, 9, 22]. In this study, higher tumor anaerobic glycolytic activity is linked with lower tumoral and peritumoral pH_i . A significant correlation was also found between tumor Lac:Pyr and the pH_i gradient from the tumor to peritumor region, with higher Lac:Pyr corresponding to a higher pHG_i . The conversion of pyruvate to lactate during anaerobic glycolysis, as measured with hyperpolarized [$1-^{13}\text{C}$]pyruvate (Lac:Pyr), more

directly captures the process of tumor acidosis and indicated a directly proportional and significant relationship with the pHG_i across the tumor to peritumor region.

Although all imaging experiments were performed in 24 h, they were in the span of 2 days, specifically, FDG-PET on day 11–13, and CEST followed by the hyperpolarized [$1-^{13}\text{C}$]pyruvate on the next day. Although this is a real limitation, all imaging was completed within 24 h for each subject, and no significant changes were found in tumor volumes as mentioned in our previous publication [13]. Since tumor pH and the glycemic environment were not identical during these measurements, this could explain the absence of significant correlations between tumor SUV from FDG-PET and tumoral and peritumoral pH_i . The tumor pH environment measured from CEST would be closer to the hyperpolarized pyruvate experiment than during FDG-PET, acquired a day prior. The sequential design of the study also gave rise to distinct glucose conditions prior to the glycolysis measurements. The absence of correlation between tumor pH_i and SUV could also be because ^{18}F -FDG-PET is sensitive to both aerobic and anaerobic glycolysis. Glucose transporters such as GLUT1 also affect the uptake of ^{18}F -FDG. Moreover, ^{18}F -FDG could also be taken up by activated inflammatory cells (microglia and tumor-associated macrophages) [23], resulting in an overestimation of tumor glycolysis. In contrast to SUV, Lac:Pyr measured with hyperpolarized [$1-^{13}\text{C}$]pyruvate MRSI is more sensitive to anaerobic glycolysis [24], often regarded as a hallmark for malignant tumors such as glioma [4, 25]. Overall, this could explain the significant correlation of tumor pH_i obtained using AACID with Lac:Pyr instead of SUV. The subjects were normoglycemic before FDG-PET, while they were hyperglycemic prior to hyperpolarized [$1-^{13}\text{C}$]pyruvate experiment as it was conducted the following day immediately after the dynamic CEST experiment. Under the effect of hyperglycemia, directly proportional relationships were found between tumor Lac:Pyr vs. tumor and peritumor ΔpH_i . A higher tumor Lac:Pyr is related to a greater shift towards the basic direction in tumor and peritumor pH_i . This could be because cells in tumoral and peritumoral regions try to maintain pH homeostasis to avoid acidosis which would result in cell death [1, 2]. The acute change could be detected using AACID CEST.

There were several limitations from this study, to follow the radiation safety protocols at different sites, the rats had to be housed at our PET facility overnight before they could be transferred to the MR facility. In the future, experiments could be carried out on a hybrid PET/MR system not only to simplify the experimental procedure but also to provide simultaneous measurements under the same tumor pH and metabolic microenvironment. Only male Wistar rats were used in this experiment [26], as the effect of sex-specific hormones such as progesterone and estradiol on glioma

progression is variable, with both protective and promoter effects depending on tumor type and hormone concentration [27]. Future studies will evaluate the interaction of pH and glucose metabolism in both male and female tumor models. The precise roles of glucose transporters were not examined in this study—histological information about these transporters will be acquired in future studies, and the correlation between the distribution of these glucose transporters and the tumor pH_i environment can then be evaluated [2, 3]. A measurement of pH_e would also aid in interpreting these results. We plan on acquiring this information in a future study simultaneously with acidoCEST [7, 9] to provide a more complete picture of the tumor pH environment. The current 60-min glucose infusion protocol leads to hyperglycemia by the end of the AACID CEST experiment. The acute change in pH_i environment after the glucose infusion was not measured in the current study due to a different CEST acquisition protocol which was used during the first half of glucose infusion. Moreover, the Lac:Pyr value obtained from the MRSI right after would be elevated under hyperglycemia [13, 28, 29]—a CEST acquisition promptly following a bolus injection of moderate dose will be implemented in the future to avoid an overly large alteration of the tumor glycolytic environment.

Conclusions

This study demonstrated that using AACID CEST MRI, a change in tumor pH_i can be detected after glucose infusion; the presence of metabolites with similar resonant frequencies with amine or amide would not significantly affect AACID, although the calibrations were distinct under different metabolite concentrations. Tracking changes in tumor pH could provide information about tumor metabolism, and pH imaging using AACID CEST MRI can be used as an alternative for tumor metabolic imaging. Hyperglycemia induced by glucose infusion leads to a change in tumoral pH_i that can be detected *in Vivo* using CEST MRI. The relationship between tumor and peritumor pH_i environment and tumor glycolysis was explored. Tumor Lac:Pyr is significantly inversely proportional to tumor and peritumoral pH_i ; it is also significantly directly proportional to tumoral and peritumoral ΔpH_i induced by a glucose infusion. The associations emphasize the innate relationship between tumor glycolytic metabolism and the tumor pH environment as well as the peritumor pH environment. A multimodal imaging approach could provide a more complete picture of the process of tumor progression and invasion by monitoring both tumor glycolysis and the change in the pH environment.

Supplementary Information The online version contains supplementary material available at <https://doi.org/10.1007/s11307-022-01726-0>.

Declarations

Conflict of Interest The authors declare that they have no conflict of interest.

References

1. Webb BA, Chimenti M, Jacobson MP et al (2011) Dysregulated pH: a perfect storm for cancer progression. *Nat Rev Cancer* 11(9):671–677. <https://doi.org/10.1038/nrc3110>
2. Corbet C, Feron O (2017) Tumour acidosis: from the passenger to the driver's seat. *Nat Rev Cancer* 17(10):577–593. <https://doi.org/10.1038/nrc.2017.77>
3. Estrella V, Chen T, Lloyd M et al (2013) Acidity generated by the tumor microenvironment drives local invasion. *Cancer Res* 73(5):1524–1535. <https://doi.org/10.1158/0008-5472.CAN-12-2796>
4. Heiden MG, Cantley LC, Thompson CB (2009) Understanding the Warburg effect: the metabolic requirements of cell proliferation. *Science* (80-) 324(5930):1029–1033. <https://doi.org/10.1126/science.1160809>
5. Stubbs M, Rodrigues L, Howe FA et al (1994) Metabolic consequences of a reversed pH gradient in rat tumors. *Cancer Res* 54(15):4011–4016
6. Lim H, Albatany M, Martínez-Santesteban F et al (2018) Longitudinal measurements of intra- and extracellular pH gradient in a rat model of glioma. *Tomography* 4(2):46–54. <https://doi.org/10.18383/j.tom.2018.00001>
7. Chen LQ, Howison CM, Jeffery JJ et al (2014) Evaluations of extracellular pH within *in Vivo* tumors using acidoCEST MRI. *Magn Reson Med* 72(5):1408–1417. <https://doi.org/10.1002/mrm.25053>
8. Volk T, Jähde E, Fortmeyer HP et al (1993) pH in human tumour xenografts: effect of intravenous administration of glucose. *Br J Cancer* 68(3):492–500. <https://doi.org/10.1038/bjc.1993.375>
9. Longo DL, Bartoli A, Consolino L et al (2016) *In Vivo* imaging of tumor metabolism and acidosis by combining PET and MRI-CEST pH imaging. *Cancer Res* 76(22):6463–6470. <https://doi.org/10.1158/0008-5472.CAN-16-0825>
10. Albatany M, Li A, Meakin S et al (2018) Dichloroacetate induced intracellular acidification in glioblastoma: *in vivo* detection using AACID-CEST MRI at 9.4 Tesla. *J Neurooncol* 136(2):255–262. <https://doi.org/10.1007/s11060-017-2664-9>
11. McVicar N, Li AX, Gonçalves DF et al (2014) Quantitative tissue pH measurement during cerebral ischemia using amine and amide concentration-independent detection (AACID) with MRI. *J Cereb Blood Flow Metab* 34(4):690–698. <https://doi.org/10.1038/jcbfm.2014.12>
12. Lim H. (2017) Tumour metabolism using hyperpolarized carbon-13 magnetic resonance spectroscopic imaging in a preclinical model of glioma. PhD Thesis
13. Qi Q, Fox MS, Lim H et al (2021) Multimodality *in Vivo* imaging of perfusion and glycolysis in a rat model of C6 glioma. *Mol Imaging Biol* 23:516–526. <https://doi.org/10.1007/s11307-021-01585-1>
14. Qi Q, Yeung TPC, Lee TY et al (2016) Evaluation of CT perfusion biomarkers of tumor hypoxia. *PLoS ONE* 11(4). <https://doi.org/10.1371/journal.pone.0153569>
15. Yeung TPC (2014) Functional imaging of malignant gliomas with CT perfusion. PhD Thesis.
16. Gallamini A, Zwarthoed C, Borra A (2014) Positron emission tomography (PET) in oncology. *Cancers* 6(4):1821–1889. <https://doi.org/10.3390/cancers6041821>

17. Silver IA, Erecinska M (1994) Extracellular glucose concentration in mammalian brain: continuous monitoring of changes during increased neuronal activity and upon limitation in oxygen supply in normo-, hypo-, and hyperglycemic animals. *J Neurosci* 14(8):5068–5076. <https://doi.org/10.1523/jneurosci.14-08-05068.1994>
18. Zaiss M, Anemone A, Goerke S et al (2019) Quantification of hydroxyl exchange of D-glucose at physiological conditions for optimization of glucoCEST MRI at 3, 7 and 9.4 Tesla. *NMR Biomed* 32(9). <https://doi.org/10.1002/nbm.4113>
19. Zaiss M, Zu Z, Xu J et al (2015) A combined analytical solution for chemical exchange saturation transfer and semi-solid magnetization transfer. *NMR Biomed* 28(2):217–230. <https://doi.org/10.1002/nbm.3237>
20. Yeung TPC, Kurdi M et al (2014) CT perfusion imaging as an early biomarker of differential response to stereotactic radiosurgery in C6 rat gliomas. *PLoS ONE* 9(10). <https://doi.org/10.1371/journal.pone.0109781>
21. McVicar N, Li AX, Suchý M et al (2013) Simultaneous *in Vivo* pH and temperature mapping using a PARACEST-MRI contrast agent. *Magn Reson Med* 70(4):1016–1025. <https://doi.org/10.1002/mrm.24539>
22. Coman D, Huang Y, Rao JU et al (2016) Imaging the intratumoral-peritumoral extracellular pH gradient of gliomas. *NMR Biomed* 29(3):309–319. <https://doi.org/10.1002/nbm.3466>
23. Roesler R, Dini SA, Isolan GR (2021) Neuroinflammation and immunoregulation in glioblastoma and brain metastases: recent developments in imaging approaches. *Clin Exp Immunol* 206(3):1–11. <https://doi.org/10.1111/CEI.13668>
24. Golman K, Zandt R, Lerche M et al (2006) Metabolic imaging by hyperpolarized ¹³C magnetic resonance imaging for *in Vivo* tumor diagnosis. *Cancer Res* 66(22):10855–10860. <https://doi.org/10.1158/0008-5472.CAN-06-2564>
25. Kroemer G, Pouyssegur J (2008) Tumor cell metabolism: cancer's Achilles' heel. *Cancer Cell* 13(6):472–482. <https://doi.org/10.1016/J.CCR.2008.05.005>
26. Nagano N, Sasaki H, Aoyagi M et al (1993) Invasion of experimental rat brain tumor: early morphological changes following microinjection of C6 glioma cells. *Acta Neuropathol* 86(2):117–125. <https://doi.org/10.1007/BF00334878>
27. Yang W, Warrington NM, Taylor SJ et al (2019) Sex differences in GBM revealed by analysis of patient imaging, transcriptome, and survival data. *Sci Transl Med* 11(473). <https://doi.org/10.1126/SCITRANSLMED.AAO5253>
28. Lund J, Ouwens DM, Wettergreen M et al (2019) Increased glycolysis and higher lactate production in hyperglycemic myotubes. *Cells* 8(9). <https://doi.org/10.3390/CELLS8091101>
29. Twarock S, Reichert C, Peter U et al (2017) Hyperglycaemia and aberrated insulin signalling stimulate tumour progression via induction of the extracellular matrix component hyaluronan. *Int J cancer* 141(4):791–804. <https://doi.org/10.1002/IJC.30776>

Publisher's Note Springer Nature remains neutral with regard to jurisdictional claims in published maps and institutional affiliations.

Springer Nature or its licensor (e.g. a society or other partner) holds exclusive rights to this article under a publishing agreement with the author(s) or other rightsholder(s); author self-archiving of the accepted manuscript version of this article is solely governed by the terms of such publishing agreement and applicable law.